

ELECTROCHEMISTRY

A 4D x-ray computer microtomography for high-temperature electrochemistry

Handong Jiao^{1†}, Zhaoliang Qu^{1†}, Shuqiang Jiao^{1,2*}, Yang Gao², Shijie Li¹, Wei-Li Song^{1*}, Haosen Chen¹, Hongmin Zhu³, Rongqi Zhu⁴, Daining Fang^{1*}

High-temperature electrochemistry is widely used in many fields. However, real-time observations and an in-depth understanding of the inside evolution of this system from an experimental perspective remain limited because of harsh reaction conditions and multiphysics fields. Here, we tackled this challenge with a high-temperature electrolysis facility developed in-house. This facility permits in situ x-ray computer microtomography (μ -CT) for nondestructive and quantitative three-dimensional (3D) imaging. In an electrorefining system, the μ -CT probed the dynamic evolution of 3D morphology and components of electrodes (4D). Subsequently, this 4D process was visually presented via reconstructed images. The results monitor the efficiency of the process, explore the dynamic mechanisms, and even offer real-time optimization. This 4D analysis platform is notable for in-depth combinations of traditional electrochemistry with digital twin technologies owing to its multiscale visualization and high efficiency of data extraction.

INTRODUCTION

High-temperature electrochemistry is widely used in the metallurgy, nuclear, chemical production, and energy industries. In metallurgy, molten salt/oxide electrolysis can extract and purify metal (1, 2); it has a potential leading role in large-scale stationary energy storage transformation (3, 4). However, experimentally probing and understanding the internal dynamic evolution of high-temperature electrochemical systems remain a major challenge and severely limit the development of high-temperature electrochemistry. For example, it is difficult to establish a mathematical model for rationally designing and optimizing the processes owing to a lack of evolution details in anode dissolution (5). In addition, the growth mechanism of deposited production is poorly understood—this is critical to effectively regulating morphology, purity, and yield of cathodic products (6). Versus the rapid development of electrochemistry (7, 8), specific experimental facilities and advanced analysis methods are urgently needed in high-temperature electrochemistry. This can be a more intuitive and quantitative methodology.

The absence of real-time facilities and strategy in high-temperature electrochemistry mainly results from the harsh reaction environment, including high temperature, corrosion, air-free, and complex multiphysics fields (temperature, concentration, and electric fields/gradients). Thus, there are multiple critical limiting conditions when developing tools that operate stably under these extreme environments. X-ray computer microtomography (x-ray μ -CT) is a promising potential technique that offers sufficient penetration ability, nondestructive sampling, and noncontact features. It has an excellent adaptability and can be combined with high-temperature electrochemical systems (9). X-ray μ -CT is a powerful in situ tool in the emerging fields of energy and material sciences owing to its

ability to image structures in three dimensions (3D) with high-spatial resolution across multiple scales. It is established in physics, biology, and medicine (10, 11). In 2013, Ritchie and co-workers (12) developed a facility that enables in situ μ -CT for measuring the solid components under tensile or compressive loads at high temperatures. Nearly concurrently, x-ray μ -CT was used in a room-temperature electrochemical system to monitor the electrode evolution in Li-ion batteries (13, 14). Recently, Chen-Wiegart and co-workers (15) used in situ 3D x-ray μ -CT to study dealloying by settling the sample in heated molten salt. Nevertheless, there is still a lack of in situ or operando techniques for investigating electrode kinetics in high-temperature electrochemical systems due to the extremely harsh operating environment; thus, parameter optimization of high-temperature electrochemical processes is unfortunately still based on empirical work (16, 17).

To achieve real-time monitoring of dynamic evolution in harsh high-temperature electrochemical systems, we developed here a specific high-temperature electrochemical facility equipped with x-ray μ -CT. This enables in situ and quantitative capture of 3D images including those of the morphology and components of the electrodes inside the electrochemical systems under extreme reaction conditions. The apparatus can perform electrochemical experiments at a stable and high temperature (up to 1000°C) in an inert or vacuum atmosphere. Along with electrochemical processes operating at high temperature, this system can simultaneously generate 3D tomograms at 6 to 10 μ m per voxel, which is sufficient for high spatial resolution and reconstruction of 4D multiscale morphological details of electrodes (i.e., 3D imaging from microscopic to macroscopic scales; time is additional dimension). Thus, electrode processes at high temperature can be quantitatively analyzed.

To verify this apparatus, we performed a classical electrorefining experiment of titanium in molten salt. A 4D study on the electrode structures and chemical components over time was performed. Using this apparatus, 3D images of the dissolution process of Ti anode and 3D evolution process of coating on the Ni cathode were presented in situ upon high-temperature electrolysis (500°C). Furthermore, the resulting current efficiencies at different electrolysis stages were used to explore the essential relation between the competitive

Copyright © 2022 The Authors, some rights reserved; exclusive licensee American Association for the Advancement of Science. No claim to original U.S. Government Works. Distributed under a Creative Commons Attribution NonCommercial License 4.0 (CC BY-NC).

¹Institute of Advanced Structure Technology, Beijing Institute of Technology, Beijing 100081, PR China. ²State Key Laboratory of Advanced Metallurgy, University of Science and Technology Beijing, Beijing 100083, PR China. ³Tohoku University, 6-6-02, Aramaki-Aza-Aoba, Aobo-ku, Sendai 980-8579, Japan. ⁴College of Engineering, Peking University, Beijing 100871, PR China.

*Corresponding author. Email: sjiao@ustb.edu.cn (S.J.); weilis@bit.edu.cn (W.-L.S.); fangdn@bit.edu.cn (D.F.)

†These authors contribute equally to this work.

mechanism of chemical/electrochemical reactions at the electrode interfaces at different electrolysis times. On the basis of a combination of quantitative local 3D morphologies of electrodes extracted from the reconstructed images and multiphysical results calculated from simulations, we present a kinetic mechanism (electric and concentration fields) on the evolution of 3D morphologic electrode structure. This was a pioneering 4D study on high-temperature electrochemistry, and a quantitative experimental methodology was established for an in situ understanding of the critical evolution issues in extreme electrochemical systems. The results can combine high-temperature electrochemistry with mathematical simulations and digital twin technologies to quantitatively design and optimize high-temperature electrochemistry.

RESULTS

In situ 4D facility of high-temperature electrochemistry

Figure 1A shows a schematic of the homemade in situ 4D characterization apparatus for high-temperature electrochemistry; more details are given in Materials and Methods. A quartz tube electrolysis cell was fixed vertically to the rotation actuator axis of the x-ray system. The molten salt medium and the electrodes were connected with an electrochemical measurement system via metal wires and sealed sealing with a homemade cap under an inert Ar atmosphere. The cell was heated by four 150-W halogen lamps fixed in the vertical plane diagonal to the heating furnace; each lamp has a hemispherical reflector facing toward the center of the cell. Under high-temperature operating conditions, the furnace chamber was settled under vacuum condition to reduce the temperature outside the furnace. Note that the distance between the halogen lamps and the cell could be matched; consequently, the area of the heated zone could be altered according to experimental requirements.

Figure 1B shows the spatial configuration of the in situ 4D electrolysis and x-ray systems. To capture the tomographic results of

the inner electrolysis cell, the quartz tube electrolysis cell rotates 180° via a rotation actuator. X-rays simultaneously penetrate through the 300- μm -thick aluminum transmission window. The heating furnace was designed to be a flat frame (Fig. 1C) and could effectively shorten the distance between the sample and x-ray source. This increases the spatial resolution of such a 4D facility. After each scan, a set of radiographs could be obtained and converted into reconstructed 3D slices using ImageJ. Figure 1D shows a photograph of the electrolysis cell; the high-temperature molten salt could be heated to 500°C according to the melting temperature of selected electrolyte media. Meanwhile, the photographs of the inner images could be captured by the optical camera through the peephole of the heating component.

The electrolysis quartz cell is optically transparent, but it remains challenging to obtain a clear view of the inner cell via an optical camera due to the thermal radiation from the high-temperature molten salt when the temperature is elevated. To capture clear images of the molten salt at high temperature, previous studies proposed alternative technologies to remove the influence of thermal radiation (18). However, the inherent shortages of optical imaging have substantially limited the high-temperature study in molten salt systems. For instance, optical images are largely distorted because of the different refractive index between air and molten salt. Complex 3D structures cannot be imaged well because of poor light penetration. In contrast, the resulting in situ 4D facility based on x-ray $\mu\text{-CT}$ technique here could reconstruct a reliable 3D complex structure of the inner electrochemical cells along with high-spatial resolution from microscopic to macroscopic scales (Fig. 1E).

4D analysis of Ti electrorefining in the molten salt medium

A typical experiment of Ti electrorefining in molten salt was performed next to demonstrate the capability of the developed in situ 4D facility for high-temperature electrochemistry. Note that extraction and purification of Ti using molten salt electrolysis have been

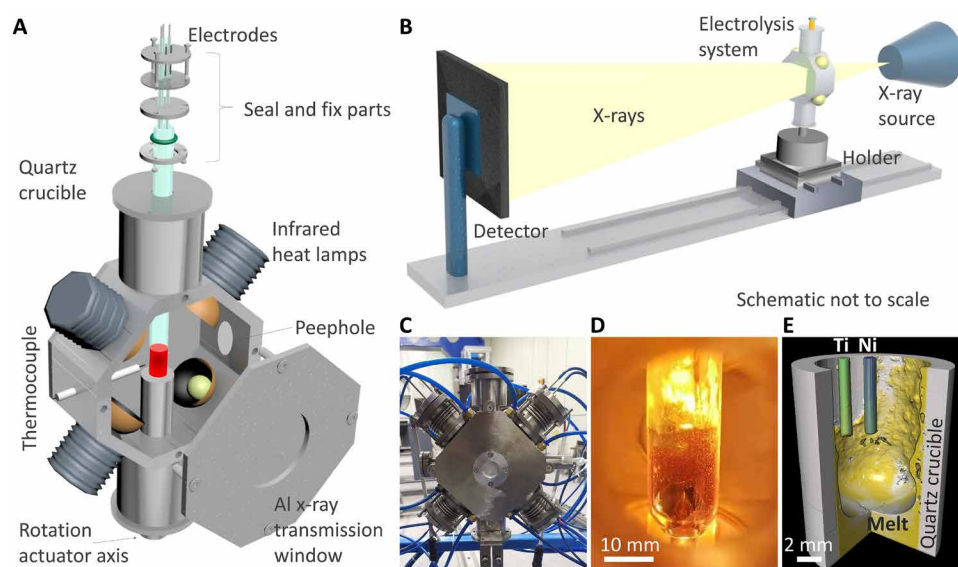


Fig. 1. Schematics and photographs of 4D imaging apparatus for high-temperature electrochemistry. (A) 3D scheme of the assembled 4D characterization facility for high-temperature electrochemistry. (B) Schematic of the facility in transmission mode for x-ray $\mu\text{-CT}$. (C) Photograph of the 4D studying facility. (D) Photograph of the high-temperature electrolysis cell through a peephole of the facility. (E) 3D reconstructed image of the experimental electrolysis cell at high temperature.

extensively studied in our group (19–21); the mechanism remains unclear on the basis of efficiency, purity, and yield data for cathodic products.

The procedures of this experiment are given in Materials and Methods. Briefly, a two-electrode system was used, and Ti and Ni wires with same area and current density were used as the anode and cathode, respectively. The 4D studies were performed under a nearly continuous condition involving scanning, electrolyzing, and repeating this process. The scan time for one tomograph is about 30 to 40 min in a laboratory-scale x-ray system. The voltage-time profiles for the electrorefining process at different current densities are 0.3 and 0.6 A cm⁻² and are shown in fig. S1. At each electrolysis stage, the profile dropped slowly in the initial stage and then was

0.2 to 0.4 V corresponding to the representative cell voltage-time profile of the Ti electrorefining process.

The reconstructed 3D images of the Ti anode (Fig. 2A) and Ni cathode (Fig. 2B) at different electrolysis time ranges are provided under two current densities of 0.3 and 0.6 A cm⁻². The gray values of Ti and Ni in each slice are different, and it is easy to distinguish these two elements (fig. S2). In this work, the Ti and Ni wires were green and violet, respectively. These 3D images show the evolution of the electrode morphologies during electrorefining process (movie S1). The dissolution loss of Ti anode is visible to the naked eye at both 0.3 A cm⁻² or at 0.6 A cm⁻² presenting nonuniform dissolution behavior. In contrast, the deposition of Ti at the Ni cathode is unobvious and remains more uniform in the morphology.

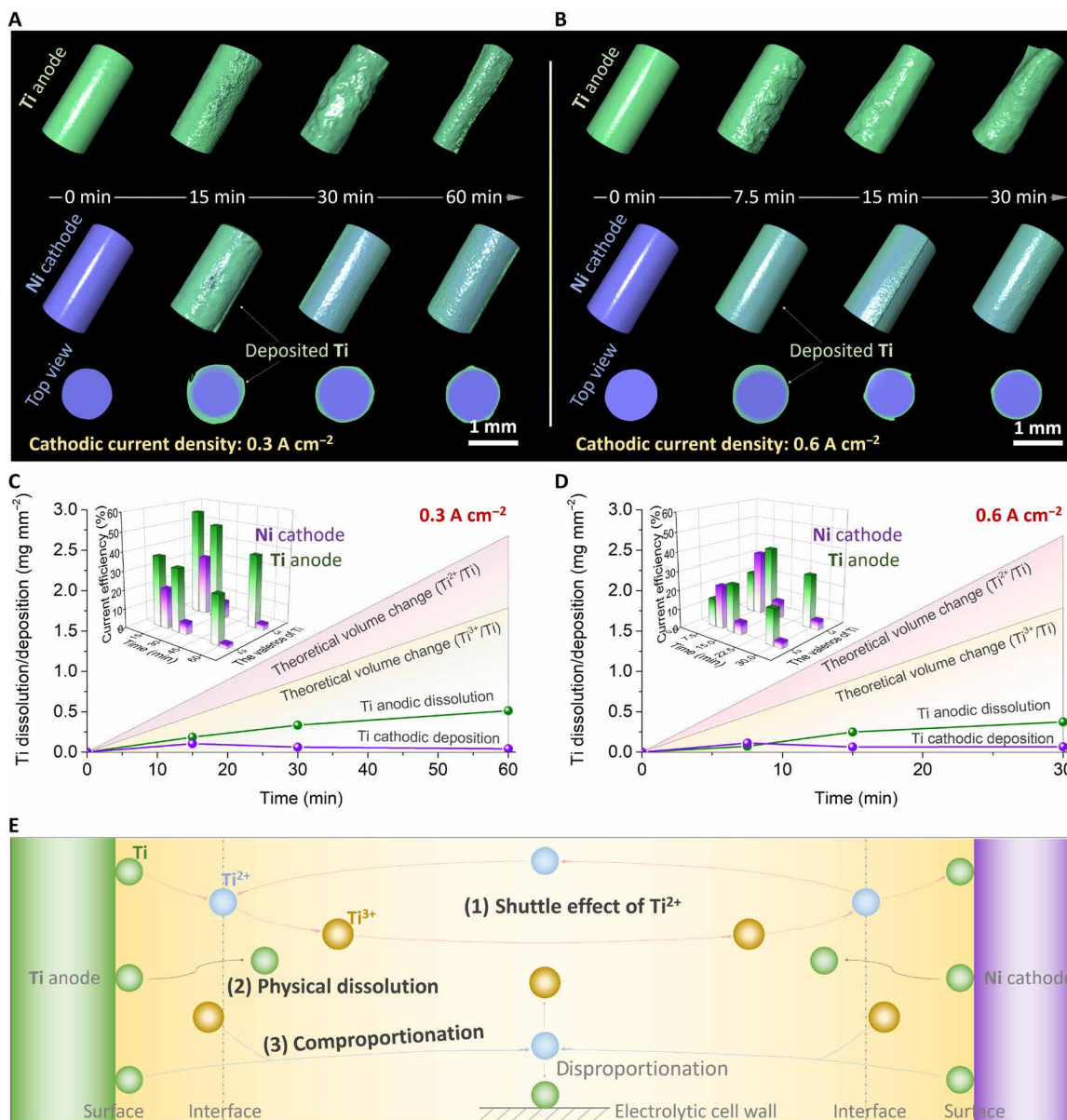


Fig. 2. 4D imaging and analysis of Ti electrorefining in the molten salt medium. (A and B) 3D reconstructed images of the Ti anode and Ni cathode at different electrolysis time ranges. Current density, 0.3 A cm⁻² (A) and 0.6 A cm⁻² (B). (C and D) The change of the dissolution mass of Ti anode and the Ti deposition mass on the Ni cathode at different electrolysis stages. The insets are current efficiencies of Ti anode and Ni cathode at different electrolysis stages. (E) The competitive mechanism of possible reactions at electrodes.

Furthermore, the fractal dimension of the electrodes has also been extracted to quantitatively analyze the roughness of those electrodes at different electrolysis stages (22). Quantitative roughness results are consistent with our visual perception, indicating that the roughness of the Ti anode is greater than that of Ni cathode after electrolysis (fig. S3). Notably, there is no obvious relationship between the roughness and electrolysis time, thus demonstrating that roughness has no pronounced time dependence on the electrolysis process.

In addition, the average thickness of the Ti anodic stripping and Ti cathodic deposition was calculated by statistical methods. The results are summarized in Fig. 2 (C and D). The insets show the current efficiencies of Ti anode and Ni cathode at different electrolysis stages. These were obtained via similar statistical methods. In both Ti anodic dissolution and Ti cathodic deposition, it is interesting that the current efficiency is far below expectations based on our previous results (19, 20). The average thickness of Ti plating on the Ni cathode increased during the first electrolysis stage. It then dropped slowly with electrolysis time, which is unusual. Such an unprecedented phenomenon encourages us to further study the competitive mechanism of chemical and electrochemical reactions at the interface/on the surface of the electrodes. Figure 2E illustrates the possible reactions or processes in this electrochemical system.

The related reactions or processes in actual Ti dissolution or deposition are listed below. Specifically, the actual mass loss of Ti anode should follow

$$m_{\text{actual}}^+ = m_{\text{theory}}^+(I, t) - m_{\text{shuttle}}^+(i^+, \text{melt}) + m_{\text{dissolve}}^+(S^+, \text{melt}, t) + m_{\text{comp}}^+(S^+, \text{melt}, t) \quad (1)$$

The actual mass increase in Ni cathode could be described as

$$m_{\text{actual}}^- = m_{\text{theory}}^-(I, t) - m_{\text{shuttle}}^-(i^-, \text{melt}) - m_{\text{dissolve}}^-(S^-, \text{melt}, t) - m_{\text{comp}}^-(S^-, \text{melt}, t) \quad (2)$$

where m_{theory}^+ and m_{theory}^- are the theoretic mass loss of Ti anode and the theoretic mass increase in Ni cathode, respectively. They are both related to the current (I) and electrolysis time (t) and, consequently, are defined as $m_{\text{theory}}^+(I, t)$ and $m_{\text{theory}}^-(I, t)$. Similarly, m_{shuttle}^+ and m_{shuttle}^- are the mass change of Ti anode and Ni cathode, respectively. These are caused by the shuttle effect of Ti^{2+} ; i^+ and i^- are the local current densities of Ti anode and Ni cathode, respectively. In addition, melt refers to the properties of the molten salt medium, including components, viscosity, temperature condition, etc.; m_{dissolve}^+ and m_{dissolve}^- are the mass change of electrodes caused by the physical dissolution of Ti atom; S^+ and S^- are the surface areas of Ti anode and Ni cathode, respectively; m_{comp}^+ and m_{comp}^- are the mass change of electrodes caused by the comproportionation of Ti and Ti^{3+} , respectively.

The main reason for decreasing the current efficiency in Ti anodic dissolution and cathodic deposition is the shuttle effect of Ti^{2+} , which is mainly caused by the coexistence of Ti^{2+} and Ti^{3+} in the melt. Titanium is a multivalent element, and there are various titanium ions in the molten salt medium, such as Ti^{2+} and Ti^{3+} . Meanwhile, the equilibrium constant between Ti^{2+} and Ti^{3+} in both electrode processes of Ti anodic dissolution and Ti cathodic deposition is variable in different melts under various conditions (23, 24).

Other reasons for the Ni cathode include physical dissolution and comproportionation of deposited Ti as well as the shuttle effect. This refers to the decrease in Ti plating thickness at the second and

third stages upon electrolysis. With increasing electrolysis time, there is an increase between the Ti anodic dissolution mass and Ti cathodic deposition mass. These indicate that the physical dissolution and comproportionation of the cathode increased with time because of the large specific surface area of deposited Ti (fig. S4), which increases the dissolution activity of Ti atom. Thus, we concluded that the main strategy for improving the current efficiency is inhibiting the shuttle effect. This is mainly dependent on regulation of the melt properties and current density.

Electrode process of Ti dissolution and deposition

The evolution mechanism was revealed by combining real-time experimental results and simulation analyses. The local evolution information about the electrodes was extracted according to the demonstration (Fig. 3A). The variation in the thickness of Ti anodic dissolution and Ti cathodic deposition surrounding the electrodes is given in Fig. 3 (B and C, respectively). The thickness variation induced from Ti anodic dissolution randomly fluctuated from the bottom to the top of the Ti anode, implying that there is no clear change along the Ti anode. In contrast, the thickness change induced by Ti plating on the Ni cathode first decreases and then increases from the bottom to the top of the Ni cathode showing an obvious edge effect during electroplating. This edge effect could be maintained at different electrolysis stages. There is no apparent variation behavior of the thickness caused by Ti plating around the Ni cathode at different angles (Fig. 3C, right). However, the thickness variation induced by the dissolved Ti anode shows a clear change law, suggesting that the thickness on the near side is larger than at the far side. These results suggest that the anodic dissolution and cathodic deposition of Ti are not uniform.

To reveal this evolution mechanism, multiphysical field simulations were used to establish the function between the thickness change (induced by Ti anodic dissolution or Ti cathodic deposition) and physical fields. Similarly, local information about the electrode surface was extracted according to the schematic diagram (Fig. 3A). Figure 3 (D to F) shows the evolution of the 3D concentration field, current density, and electric field surrounding the electrode along with electrolysis time, respectively. The extended 3D evolution results on those evolution processes can be found in the Supplementary Materials (figs. S5 to S7 and movies S2 to S4).

The concentration is initially uniformly distributed on the surface of the Ti anode, but it generally evolves into a nonuniform distribution with electrolysis time. Therefore, the concentration at the near side of the Ti anode is higher than that at the far side. The current density has a nonuniform distribution at the initial stage, i.e., the current density at the near side is higher than the far side. Although the local current density decreases slowly with electrolysis time, the nonuniform distribution phenomenon remains unchanged. A similar evolution process is shown in the electric field, but the likelihood is opposite. In contrast, the concentration, the current density, and the electric field do not have distinct behavior along the vertical direction. There is obviously a strong correlation between the thickness evolution of Ti anodic dissolution and distribution features of these physical fields. Consequently, the mechanism for the nonuniformity of the Ti anodic stripping is mainly induced by evolution of physical fields upon high-temperature electrolysis.

Likewise, the evolution of the 3D physical fields surrounding the Ni cathode was also monitored as given in Fig. 3 (G to I). At the

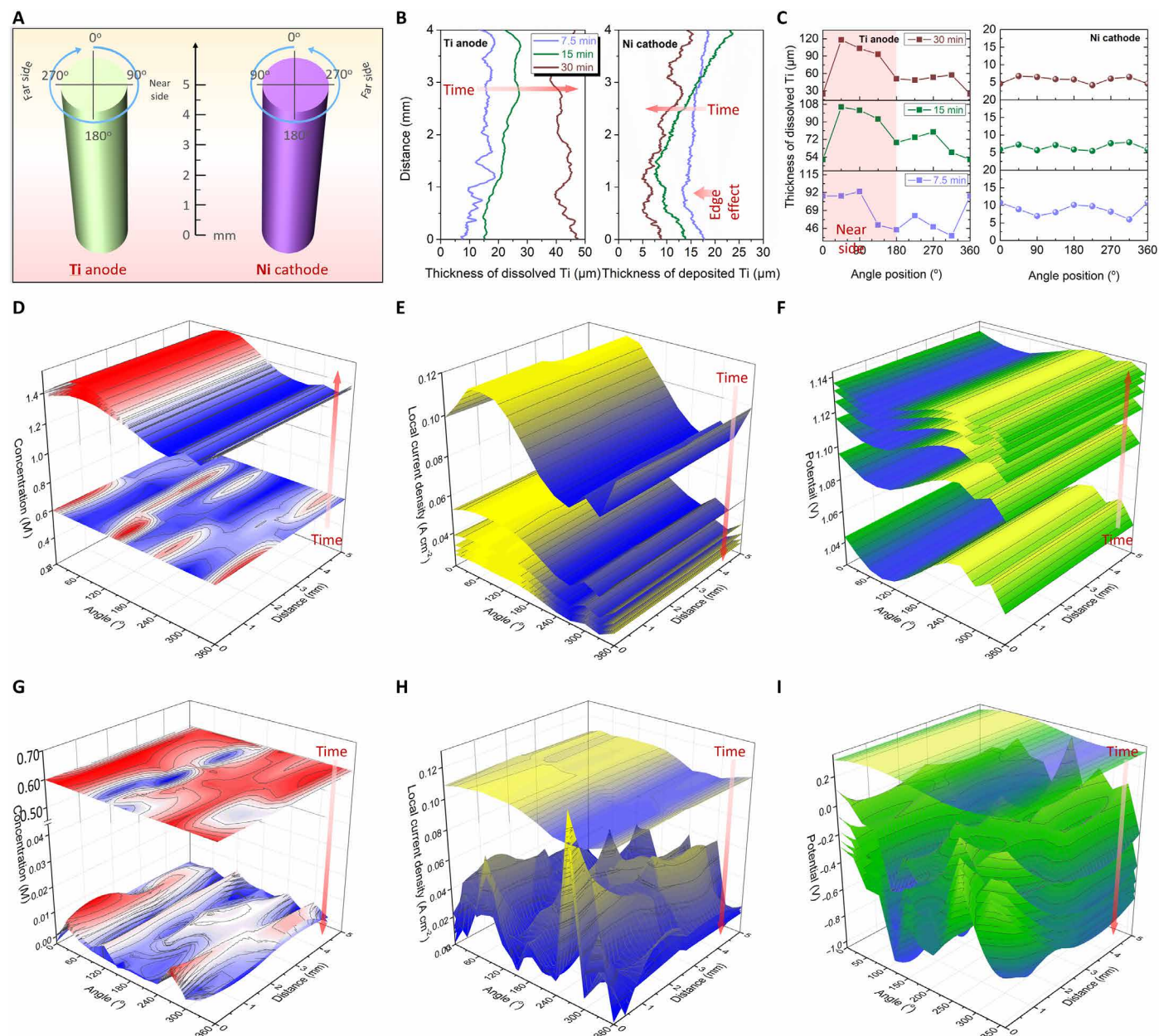


Fig. 3. 4D evolution process and mechanism of Ti electrorefining. (A) Demonstration of electrode surface information extraction. (B) The evolution processes of the thickness of the dissolved Ti (left) and the deposited Ti (right) from the bottom to the top of the electrodes as obtained from the 3D reconstructed images. (C) The evolution processes of the thickness of the dissolved Ti (left) and the deposited Ti (right) on different angles of electrodes obtained from 3D reconstructed images. (D to F) The evolution of concentration field, electric field, and current density on the surface of the Ti anodes calculated from the simulation results. (G to I) The evolution of concentration field, electric field, and current density on the surface of the Ni cathode calculated from simulation results.

initial stage, namely, before the electrolysis, the distribution behaviors of concentration, current density, and electric field surrounding the Ni cathode are similar to those in the Ti anode. However, they present different evolution processes in the following high-temperature electrolysis. In contrast to the uniform distribution of physical fields along the vertical direction of the Ti anode, all the physical fields, including concentration field, current density, and electric field, are not uniform along vertical direction of the Ni cathode with increasing electrolysis time. Meanwhile, the local current density near the bottom of the Ni cathode is higher than that near the middle section

of the Ni cathode, which may result in edge effects at the Ni cathode. There are no obvious distribution laws at the near side or far side, suggesting that the physical field distribution is not the same function as the angular position. This conclusion agrees with the uniform distribution of Ti plating around the Ni cathode. As a result, the evolution of Ti stripping or plating during electrorefining is strongly connected with the distribution of local physical field around the electrodes. This is apparently an essential pathway to regulate the distribution of those fields and achieve homogeneous stripping or plating.

Process optimization based on 4D analysis

A preliminary attempt was made to optimize the electrorefining process in situ based on our 4D characterization facility. This attempt was based on understanding of the electrochemical behavior from in situ 4D observation and quantitative analysis of the electrode process. In this section, a previously less used electrolysis system with a Ti sheet rolled into a cylinder (8 mm in diameter) was used as the anode, and a Ni wire as cathode was placed in the center of the rolled Ti anode (Fig. 4A). The symmetrical arrangement of the electrolysis system leads to uniform local physical fields around the Ni cathode versus the electrolysis configuration in Fig. 1E. This step is expected to improve the quality of the deposited products.

Figure 4B presents the 3D geometric evolution of both the Ti cylinder anode and Ni wire cathode during electrolysis; the dissolution of the Ti anode was very severe after 2 hours of electrolysis under a cathodic current density of 0.2 A cm^{-2} (the corresponding

initial anodic current density was 0.025 A cm^{-2}). Meanwhile, the cell voltage obtained from the second electrolysis stage was higher than the first electrolysis stage owing to a decrease in the Ti anode area (Fig. 4C). The edge effect was also detected from the Ni cathode in the initial 2 hours of electrolysis, indicating that the local physical fields distribution is nonuniform (Fig. 4D). To compensate for the decrease in Ti anode area and to make the physical fields uniform around the Ni cathode, the Ti anode area was altered by increasing the immersion depth/volume of the Ti anode. Figure 4C shows that the cell voltage remarkably decreases after in situ anode position optimization; the edge effect was efficiently inhibited by this optimization.

Furthermore, the current efficiency of the Ti cathodic deposition was monitored statistically (Fig. 4E). The change in the current efficiency is similar to the results mentioned above. These were obtained from the first configuration (Fig. 1E). The current efficiency

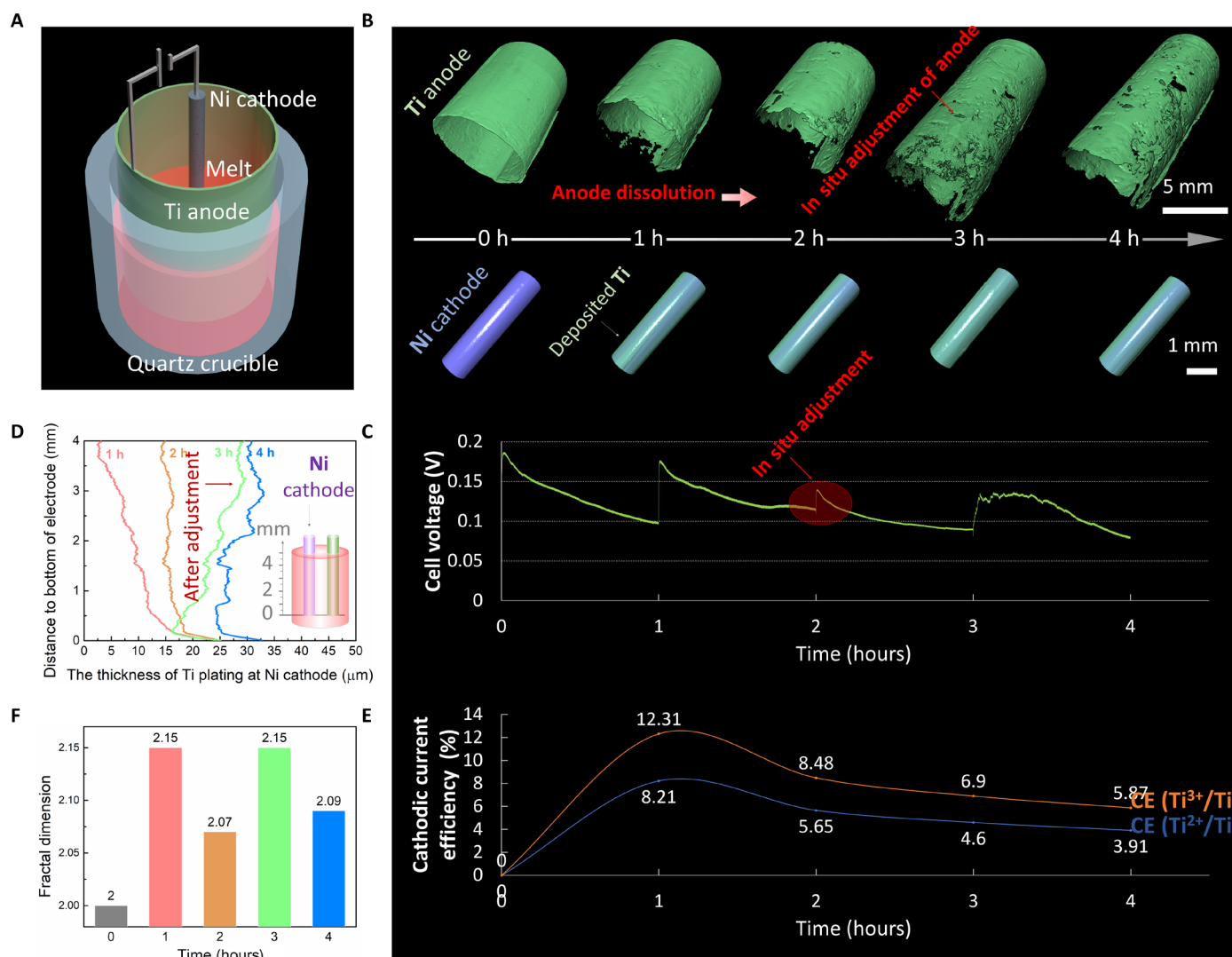


Fig. 4. In situ optimization of Ti refining process. (A) 3D views of the novel electrolysis system of Ti refining. (B) 3D reconstructed images of the Ti anode and Ni cathode at different electrolysis time ranges. Current density, 0.2 A cm^{-2} . (C) Cell voltage-time profile of electrolysis process. (D) The evolution process of the thickness of the deposited Ti from the bottom to the top of the Ni cathode obtained from 3D reconstructed images. (E) The current efficiency of the Ti cathodic deposition on a Ni cathode at different electrolysis stages. (F) The roughness of the Ni cathode at different electrolysis time spans.

increased in the first electrolysis stage and then dropped slowly with electrolysis time. However, the average thickness of Ti plating on the Ni cathode constantly increases during electrolysis. This is better than the values via the first configuration. These findings indicate that the novel electrolysis configuration with a symmetrical arrangement is significant for improving the yield of cathodic products. Last, the roughness of the Ni cathode was studied by calculating the fractal dimensions (Fig. 1F). The results show that the roughness randomly fluctuates during electrolysis, thus indicating that the morphology change of the Ni electrode was small. This conclusion was further supported by the reconstructed 3D images of the Ni cathode, where a smooth surface appeared on the Ni cathode surface with a spatial resolution of 6 to 10 μm . Scanning electron microscopy (SEM) images and EDS results of the Ni cathode after electrolysis for 4 hours are shown in figs. S8 and S9. Those results demonstrate that the Ti plating (with a thickness in the range from 11 to 45 μm) on the Ni cathode is relatively smooth and agrees with the x-ray tomography data.

DISCUSSION

In summary, this exploratory work successfully developed an in situ x-ray μ -CT technique for high-temperature electrochemistry. The product offers novel 4D characterization of high-temperature electrochemistry. A Ti electrorefining experiment at high temperature was used to verify the concept. With this 4D method, the evolution of electrolysis could be monitored in situ for quantitative data on electrode morphologies and current efficiency of both anodic dissolution and cathodic deposition at different electrolysis stages. By combining the quantitative 4D experimental results and the multiphysical simulation results, the mechanism of local physical fields on the evolution process could be understood in detail. Moreover, in situ process optimization was used to improve the high-temperature electrolysis. Overall, this technique could be widely extended into high-temperature electrochemical systems and industries. It can lead to substantial development and use cutting-edge techniques from information technology.

MATERIALS AND METHODS

Materials and chemicals

Following procedures previously described in (25), NaCl, KCl, and LiCl (99.9%) were purchased from Alfa Aesar. Anhydrous titanium tetrachloride (TiCl_4 , 99.99%) were purchased from Tokyo Chemical Industry. Ni wire (99%, 1 mm in diameter), Ti wire (99.9%, 1 mm in diameter), and Ti sheet wire (99%, 0.2 mm in thickness) were from Aladdin. All metallic electrodes were polished by gauze and then cleaned by anhydrous alcohol before the experiments. The LiCl-NaCl-KCl eutectic melt [35.4-15.4-49.2 weight % (wt %)] with 4.5 wt % TiCl_x ($2 \leq x \leq 3$) was mixed in a glove box under an inert atmosphere and then placed into a quartz tube used as the electrolysis cell. The mixed electrolyte was predried under vacuum at 200°C for 48 hours. All experiments were conducted in a sealed vessel under Ar atmosphere at 500°C, and the temperature was measured by a thermocouple (protected by a steel tube) inserted into the melt (25).

In situ 4D electrolytic cell

The in situ 4D electrolytic cell mainly consists of two parts. Part one is the electrolytic cell made from a quartz tube (inner diameter,

14 mm) with a steel cap—this was fixed vertically to the rotation actuator axis of the x-ray system. Part two is the heating furnace that surrounded the electrolytic cell and was heated by four halogen lamps. To increase the spatial resolution of the facility, the heating furnace was designed to be a flat shape and could reduce the distance between the x-ray source and the melt. Consequently, this facility can provide a 6- to 10- μm spatial resolution to reveal the dynamic evolution process of the electrode structure and morphology in high-temperature electrochemical system. A two-electrode setup was used for in situ 4D studies of Ti electrorefining. Two electrode arrangement modes were developed: In the first mode, the Ti and Ni wires were used as anode and cathode, respectively, with the same initial area. In the second mode, a Ti sheet was rolled into an 8-mm-diameter cylinder as the anode, and Ni wire was the cathode (25).

Electrochemical measurements and materials characterizations

The potentiostatic electrodeposition was conducted in the electrolytic cell with a CHI electrochemical workstation (660E, Shanghai Chenhua Instrument Co. Ltd.) at 500°C. Two current densities were used in the first electrode mode: 0.3 and 0.6 A cm^{-2} . Meanwhile, to confirm that the electric energy at different current densities is equal, the durations for electrorefining were 30 and 15 min. The cathodic current density was set to 0.2 A cm^{-2} in the second electrolysis mode, and electrolysis time was 4 hours. The Ni electrodes after electrolysis for 30, 15, and 4 hours were 0.3, 0.6, and 0.2 A cm^{-2} , respectively. The electrodes were taken out of the melt and washed with anhydrous ethanol to remove any residual electrolyte. The collected Ni electrodes were characterized by SEM (JSM-6701F, JEOL) equipped with an EDS probe (NS7, Thermo Fisher Scientific) (25).

In situ x-ray tomography

The electrolytic cell with a heating furnace was fixed vertically to the holder of laboratory x-ray system (nanoVoxel-4000, China Tianjin Sanying Precision Instrument Co. Ltd.) as shown in Fig. 1B. The scans were conducted with x-rays at 30 kV and 0.5 mA. The 3D information was collected in 800 to 1500 cross-sectional slices, and each slice was separated by one spatial resolution. The collected 3D data were then reconstructed using Avizo software. The initial 3D result was obtained by scanning the original Ti anode and Ni cathode without electrolysis. The second 3D results were collected by scanning the electrodes after electrorefining. As an analogy, we eventually got the dynamic evolution of 3D morphology and material components of Ti anodes and Ni cathodes during electrorefining (25).

Modeling and simulation

A COMSOL Multiphysics simulation was performed to model and simulate the evolution of the Ti electrorefining. The physics model “tertiary current distribution and Nernst-Planck(tcd)” was used. The Nernst-Planck equation in the COMSOL Multiphysics simulation is shown as follows

$$J_i = -D_i \nabla c_i - z_i u_{m,i} F c_i \nabla \varphi_i \quad (3)$$

$$\sum_i z_i c_i = 0 \quad (4)$$

$$u_{m,i} = \frac{D_i}{RT} \quad (5)$$

where J_i is the reaction flux of the ionic species, D_i is the diffusion coefficient, c_i is the concentration of reactive ions, z_i is the valence, $u_{m,i}$ is the mobility, F is the Faraday constant, and ϕ_i is the electrolyte potential.

A two-electrode system was used in the simulation process; Ni is the cathode, and Ti is the working electrode. The depth of the two electrodes immersed in the salt was 5 mm. The balance voltage distribution of cathode and anode was -1.76 and 1.76 V. The balance current of Ni and Ti electrodes was about 200 A m^{-2} . The diffusion coefficient of electrolyte ions was set to $2.72 \times 10^{-6} \text{ cm}^2 \text{ s}^{-1}$ in this molten salt system. The initial electrolyte concentration was 0.6 M . All parameters were derived from experimental results, and COMSOL was used for simulation after setting the boundary conditions.

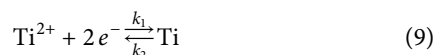
The Butler-Volmer equation was used to analyze the electrochemical process of Ti refining when setting the boundary conditions for the Ti deposition process. On the basis of the literature and our previous research results, the mechanism of reducing Ti^{3+} to Ti metal is more likely to take place in two steps: Ti^{3+} to Ti^{2+} and Ti^{2+} to Ti metal in chloride melts (26–31). Therefore, the deposition mechanism was estimated as follows: $\text{Ti}^{3+} + e^- = \text{Ti}^{2+}$ and $\text{Ti}^{2+} + 2e^- = \text{Ti}$. When simulating the process of dissolution and deposition on the electrode surface, “concentration-dependent kinetics” were selected for simulation. Parameter settings were used for experimental results. The equation was written as follows

$$i_{\text{loc}} = i_0 \left(C_{\text{O}} e^{\frac{\alpha_e F \eta}{RT}} - C_{\text{R}} e^{-\frac{\alpha_r F \eta}{RT}} \right) \quad (6)$$

where i_0 is the exchange current density, C_i is the concentration, F is the Faraday constant, α is the transfer coefficient, and η is the overpotential

$$C_{\text{O}} = \frac{k_1}{k_2} C_{\text{Ti}^{2+}} \quad (7)$$

The reactions on the cathode can be simplified as follows



The overall reaction equation at the cathode can be simplified as follows



The reaction of $\text{Ti}^{3+} + e^- \xrightleftharpoons[k_2]{k_1} \text{Ti}^{2+}$ is so facile that it is always at equilibrium relative to reaction of $\text{Ti}^{2+} + 2e^- \xrightleftharpoons[k_2]{k_1} \text{Ti}$. Thus, there is an equation $k_1 C_{\text{Ti}^{3+}} = k_2 C_{\text{Ti}^{2+}}$.

The Nernst equation of the reaction of $\text{Ti}^{2+} + 2e^- \xrightleftharpoons[k_2]{k_1} \text{Ti}$ is

$$E = E^\theta + \frac{RT}{nF} \ln \frac{C_{\text{O}}}{C_{\text{R}}} = E^\theta + \frac{RT}{nF} \ln \frac{C_{\text{Ti}^{3+}}}{C_{\text{Ti}}} = E^\theta + \frac{RT}{nF} \ln \text{Ti}^{2+} \quad (11)$$

The net reaction rate is

$$v_{\text{net}} = k_{\text{f}} C_{\text{Ti}^{3+}} - k_{\text{b}} C_{\text{Ti}} = i_{\text{nFA}} \quad (12)$$

Now consider the special case in which the interface is at equilibrium with a solution. In this situation, $E = E^\theta$ and $C_{\text{Ti}^{2+}} = C_{\text{Ti}}$, so that $k_{\text{f}} C_{\text{Ti}^{2+}} = k_{\text{b}} C_{\text{Ti}}$ and $k_{\text{f}} = k_{\text{b}}$.

The forward and reverse rate constants have the same value k_0 , so $k_{0\text{f}} = k_{0\text{b}} = k_0$

$$k_{\text{f}} = k_0 e^{-\alpha_{\text{f}} f(E-E^\theta)} \quad (13)$$

$$k_{\text{b}} = k_0 e^{(1-\alpha_{\text{r}}) f(E-E^\theta)} \quad (14)$$

$$f = nF/RT \quad (15)$$

Insertion of these relations into the equation of $v_{\text{net}} = k_{\text{f}} C_{\text{Ti}^{2+}} - k_{\text{b}} C_{\text{Ti}} = i_{\text{nFA}}$ yields the complete current-potential characteristic

$$i = nFA k_0 \left[C_{\text{Ti}^{2+}} e^{-\alpha_{\text{f}} f(E-E^\theta)} - C_{\text{Ti}} e^{(1-\alpha_{\text{r}}) f(E-E^\theta)} \right] \quad (16)$$

Insertion of the equation of $k_1 C_{\text{Ti}^{3+}} = k_2 C_{\text{Ti}^{2+}}$ into the equation above shows that the relation between current and overpotential can be written as follows

$$i = nFA k_0 \left[k_1/k_2 C_{\text{Ti}^{3+}} e^{-\alpha_{\text{f}} f(E-E^\theta)} - C_{\text{Ti}} e^{(1-\alpha_{\text{r}}) f(E-E^\theta)} \right] \quad (17)$$

where the deposition rate of Ti on the Ni electrode was given in the software. The model grid deformation at the negative electrode was described in real time and represents the morphology evolution

$$R_{\text{deposited}} = \frac{M i_{\text{loc}}}{\rho nF} \quad (18)$$

where M is the molar mass and ρ is the density of Ti (25).

SUPPLEMENTARY MATERIALS

Supplementary material for this article is available at <https://science.org/doi/10.1126/sciadv.abm5678>

REFERENCES AND NOTES

- X. Zou, L. Ji, J. Ge, D. R. Sadoway, T. Y. Edward, A. J. Bard, Electrodeposition of crystalline silicon films from silicon dioxide for low-cost photovoltaic applications. *Nat. Commun.* **10**, 5772 (2019).
- G. Z. Chen, D. J. Fray, T. W. Farthing, Direct electrochemical reduction of titanium dioxide to titanium in molten calcium chloride. *Nature* **407**, 361–364 (2000).
- K. Wang, K. Jiang, B. Chung, T. Ouchi, P. J. Burke, D. A. Boysen, D. R. Sadoway, Lithium–antimony–lead liquid metal battery for grid-level energy storage. *Nature* **514**, 348–350 (2014).
- H. Yin, B. Chung, F. Chen, T. Ouchi, J. Zhao, N. Tanaka, D. R. Sadoway, Faradaically selective membrane for liquid metal displacement batteries. *Nat. Energy* **3**, 127–131 (2018).
- P. Sarfo, A. Das, C. Young, Extraction and optimization of neodymium from molten fluoride electrolysis. *Sep. Purif. Technol.* **256**, 117770 (2021).
- H. Jiao, W. L. Song, H. Chen, M. Wang, S. Jiao, D. Fang, Sustainable recycling of titanium scraps and purity titanium production via molten salt electrolysis. *J. Clean. Prod.* **261**, 121314 (2020).
- Y. Bi, J. Tao, Y. Wu, L. Li, Y. Xu, E. Hu, J. Xiao, Reversible planar gliding and microcracking in a single-crystalline Ni-rich cathode. *Science* **370**, 1313–1317 (2020).
- J. Huang, D. B. Grys, J. Griffiths, B. de Nijs, M. Kamp, Q. Lin, J. J. Baumberg, Tracking interfacial single-molecule pH and binding dynamics via vibrational spectroscopy. *Sci. Adv.* **7**, eabg1790 (2021).
- P. J. Withers, C. Bouman, S. Carmignato, V. Cnudde, D. Grimaldi, C. K. Hagen, S. R. Stock, X-ray computed tomography. *Nat. Rev. Methods Primers* **1**, 18 (2021).
- A. Ale, V. Ermolayev, E. Herzog, C. Cohrs, M. H. De Angelis, V. Ntziachristos, FMT-XCT: In vivo animal studies with hybrid fluorescence molecular tomography–x-ray computed tomography. *Nat. Methods* **9**, 615–620 (2012).

11. H. Lusic, M. W. Grinstaff, X-ray-computed tomography contrast agents. *Chem. Rev.* **113**, 1641–1666 (2013).
12. H. A. Bale, A. Haboub, A. A. MacDowell, J. R. Nasiatka, D. Y. Parkinson, B. N. Cox, R. O. Ritchie, Real-time quantitative imaging of failure events in materials under load at temperatures above 1,600 °C. *Nat. Mater.* **12**, 40–46 (2013).
13. X. Lu, A. Bertei, D. P. Finegan, C. Tan, S. R. Daemi, J. S. Weaving, P. R. Shearing, 3D microstructure design of lithium-ion battery electrodes assisted by x-ray nano-computed tomography and modelling. *Nat. Commun.* **11**, 2079 (2020).
14. T. M. Heenan, A. V. Llewellyn, A. S. Leach, M. D. Kok, C. Tan, R. Jervis, P. R. Shearing, Resolving Li-ion battery electrode particles using rapid lab-based x-ray nano-computed tomography for high-throughput quantification. *Adv. Sci.* **7**, 2000362 (2020).
15. X. Liu, A. Ronne, L. C. Yu, Y. Liu, M. Ge, C. H. Lin, Y. C. K. Chen-Wiegart, Formation of three-dimensional bicontinuous structures via molten salt dealloying studied in real-time by in situ synchrotron x-ray nano-tomography. *Nat. Commun.* **12**, 3441 (2021).
16. Y. T. Jee, M. Park, S. Cho, J. I. Yun, Selective morphological analysis of cerium metal in electrodeposit recovered from molten LiCl-KCl eutectic by radiography and computed tomography. *Sci. Rep.* **9**, 1346 (2019).
17. L. D. Brown, R. Abdulaziz, B. Tjaden, D. Inman, D. J. L. Brett, P. R. Shearing, Investigating microstructural evolution during the electroreduction of UO₂ to U in LiCl-KCl eutectic using focused ion beam tomography. *J. Nucl. Mater.* **480**, 355–361 (2016).
18. Y. Huang, Z. Wang, Y. Yang, B. Gao, Z. Shi, X. Hu, Anodic bubble behavior in a laboratory scale transparent electrolytic cell for aluminum electrolysis. *Metals* **8**, 806 (2018).
19. S. Jiao, H. Zhu, Novel metallurgical process for titanium production. *J. Mater. Res.* **21**, 2172–2175 (2006).
20. X. Ning, H. Åsheim, H. Ren, S. Jiao, H. Zhu, Preparation of titanium deposit in chloride melts. *Metall. Mater. Trans. B* **42**, 1181–1187 (2011).
21. J. Song, Q. Wang, J. Wu, S. Jiao, H. Zhu, The influence of fluoride ions on the equilibrium between titanium ions and titanium metal in fused alkali chloride melts. *Faraday Discuss.* **190**, 421–432 (2016).
22. S. R. Nayak, J. Mishra, G. Palai, Analysing roughness of surface through fractal dimension: A review. *Image Vision Comput.* **89**, 21–34 (2019).
23. J. X. Song, Q. Y. Wang, G. J. Hu, X. B. Zhu, S. Q. Jiao, H. M. Zhu, Equilibrium between titanium ions and high-purity titanium electrorefining in a NaCl-KCl melt. *Int. J. Miner. Metall. Mater.* **21**, 660–665 (2014).
24. Q. G. Weng, R. D. Li, T. C. Yuan, L. I. Jian, Y. H. He, Valence states, impurities and electrocrystallization behaviors during molten salt electrorefining for preparation of high-purity titanium powder from sponge titanium. *Trans. Nonfer. Metal. Soc.* **24**, 553–560 (2014).
25. H. Jiao, Z. Qu, S. Jiao, Y. Gao, S. Li, W. Song, M. Wang, H. Chen, D. Fang, Quantificational 4D visualization of industrial electrodeposition. *Adv. Sci.* **8**, 2101373 (2021).
26. S. Jiao, X. Ning, K. Huang, H. Zhu, Electrochemical dissolution behavior of conductive TiC_xO_{1-x} solid solutions. *Pure Appl. Chem.* **82**, 1691–1699 (2010).
27. G. M. Haarberg, W. Rolland, Å. Sterten, Electrodeposition of titanium from chloride melts. *J. Appl. Electrochem.* **23**, 217–224 (1993).
28. E. Chassaing, F. Basile, G. Lorthioir, Study of Ti (III) solutions in various molten alkali chlorides. I. Chemical and electrochemical investigation. *J. Appl. Electrochem.* **11**, 187–191 (1981).
29. A. M. Martinez, Y. Castrillejo, E. Barrado, A chemical and electrochemical study of titanium ions in the molten equimolar CaCl₂+NaCl mixture at 550°C. *J. Electroanal. Chem.* **449**, 67–80 (1998).
30. F. Lantelme, K. Kuroda, A. Barhoun, Electrochemical and thermodynamic properties of titanium chloride solutions in various alkali chloride mixtures. *Electrochim. Acta* **44**, 421–431 (1998).
31. Y. Song, S. Jiao, L. Hu, Z. Guo, The cathodic behavior of Ti (III) ion in a NaCl-2CsCl melt. *Metall. Mater. Trans. B* **47**, 804–810 (2016).

Acknowledgments

Funding: We acknowledge financial support from the National Natural Science Foundation of China (nos. 51725401, 51874019, 51904030, 12027901, and 52074036), the Fundamental Research Funds for the Central Universities (FRF-TP-17-002C2), and Technology Innovation Program of Beijing Institute of Technology (no. 2019CX01021), Beijing Institute of Technology Research Fund Program for Young Scholars (no. 1740011182102), and BIT Teli Young Fellow.

Author contributions: S.J., W.-L.S., D.F., H.Z., and H.J. conceived the concept. H.J. and Z.Q. carried out the experiment. Y.G. performed the COMSOL simulations. W.-L.S., H.C., R.Z., and H.J. cowrote the manuscript. S.L. and H.J. carried out the characterizations. All the authors discussed the results. **Competing interests:** The authors declare that they have no competing interests. **Data and materials availability:** All data needed to evaluate the conclusions in the paper are present in the paper and/or the Supplementary Materials.

Submitted 26 September 2021

Accepted 16 December 2021

Published 9 February 2022

10.1126/sciadv.abm5678